

Physics-Informed Deep Reversible Regression Model for Temperature Field Reconstruction of Heat-Source Systems

Zhiqiang Gong, Weien Zhou, Jun Zhang, Wei Peng, and Wen Yao

Abstract—Temperature monitoring during the life time of heat source components in engineering systems becomes essential to ensure the normal work and even the long working life of the heat sources. However, prior methods, which mainly use the interpolate estimation, require large amounts of temperature tensors for an accurate estimation. To solve this problem, this work develops a novel physics-informed deep surrogate models for temperature field reconstruction. First, we defines the temperature field reconstruction task of heat-source systems. Then, this work develops the deep surrogate model mapping for the proposed task. Finally, considering the physical properties of heat transfer, this work proposes four different losses and joint learns the deep surrogate model with these losses. Experimental studies have conducted over typical two-dimensional heat-source systems to demonstrate the effectiveness and efficiency of the proposed physics-informed deep surrogate models for temperature field reconstruction.

Index Terms—Temperature Field Reconstruction of Heat Source Systems (TFR-HSS), Deep Reversible Regression Model, Physics-informed Deep Learning.

I. INTRODUCTION

Heat management plays an important role in heat-source systems where heat may be generated internally, especially over systems with electronic devices of smaller size and higher power density [1], [2]. It further affect the performance, or even the life time of the system. Temperature monitoring, which can monitor and provide the real-time operating temperature, tends to be an irreplaceable process in heat management system. Generally, temperature transducer [3], [4] is used as the engineering device to convert the temperature information to available signal as output. However, due to the high design cost, only limited number of transducers can be applied for monitoring. This would increase the difficulty to obtain the whole temperature field of the heat-source systems. Therefore, researches on *Temperature field reconstruction task of heat-source systems (TFR-HSS)* [5], [6] tend to be an important and necessary task in engineering systems, such as satellite working status, for accurate heat management.

Traditional methods utilize the interpolation method for temperature field reconstruction[7]. Interpolation is a type of estimation to reconstruct the temperature of interest area

Manuscript received XX, 2021; revised XX, 2021. This work was supported by the Natural Science Foundation of China under Grant 62001502, 52005505.

Z. Gong, W. Zhou, J. Zhang, W. Peng, W. Yao are with the National Innovation Institute of Defense Technology, Chinese Academy of Military Science, Beijing 100000, China. e-mail: (gongzhiqiang13@nudt.edu.cn, weienzhou@outlook.com, jun-zhan19@mails.tsinghua.edu.cn, wendy0782@126.com).

within the range of a discrete set of known observation temperature points, such as the linear interpolation, polynomial interpolation, spline interpolation[8]. These interpolation methods are generally fast to calculate and easy to operate. However, they cannot be adaptive to learn the correlation between the interest points and the monitoring points. Besides, they ignore the physical characteristics of the temperature field and thus usually provide the constructed temperature field with high predicted errors.

Therefore, most of the researches take advantage of surrogate modeling based on traditional regression models, such as Kriging method [9], [10], polynomial regression [11], GRBF-based kernel regression [12], gappy proper orthogonal decomposition (GOP) [13], in the literature of field reconstruction. Nevertheless, these methods which consist of limited number of parameters cannot be applied to the ultra-dimensional TFR-HSS task. Therefore, exploring surrogate models with higher representational ability and better perfomrance in describing linear and nonlinear physical information is urgent for the current ultra-dimensional task.

In recent years, deep neural networks (DNNs), as a nonlinear ultra-dimensional fitting, have achieved good performance in extracting high-level information in many fields, such as image classification [14], [15]. As a representative, convolutional neural networks (CNNs), which can extract both the local and global information and describe the complex physical correlation between different input pixels, have been applied in thermal analysis of electronic systems [16]. For the current task, considering the ultra-dimension and nonlinear physical characteristics of the mapping between observation data to temperature field, deep models with potential ability to learn the latent complex physical correlation is considered. Besides, due to the good performance, the CNN would be used as the deep surrogate model for the mapping.

However, there exist two difficulties faced in applying deep surrogate models in TFR-HSS task.

- A proper deep surrogate model which can capture physical characteristics is required to reconstruct the temperature field from obtained observation points.
- General CNN is data-driven where large amounts of labeled samples are required for the training of the deep model. However, for TFR-HSS task, the temperature field of the given observation points is expensive to obtain, sometimes even unavailable.

These problems in TFR-HSS would make it more challenging to apply deep surrogate models for TFR-HSS task.

Faced with the first problem, this work models the electronic board as a two-dimensional plane and is then formulated as a 2-D matrix, and then the reconstruction task is transformed as the mapping from the matrix of observation points to the matrix of the whole temperature field. Then, the mapping for the temperature field reconstruction can be solved by the deep regression models, such as FPN, FCN.

To solve the latter one, this work constructs the training criterion with the physical characteristics and develops the physics-informed deep learning for the TFR-HSS task. Generally, model-based deep learning methods, which can use the model prior of the data for the training of the deep model, is an effective way for the deep learning with limited samples [17], [18]. For the current task, physics properties of the thermal conduction can be used as the model prior for the training of the deep surrogate model.

To satisfy the heat transfer property, this work develops the Laplace loss which constraints the predicted temperature field with the steady-state conduction equation with heat sources. Besides, the boundary conditions is constrained by the formulated BC loss. Besides, the temperature from the observation points is mapping to the same in the reconstructed temperature field. More importantly, the total variation loss is used to force the spatial smoothness of the reconstructed temperature field. These four constructed physical losses encourage the deep surrogate model to learn the physical correlation and hence provide impressive reconstruction performance.

Considering the merits of deep surrogate model and physics-informed deep learning, this work develops a novel physics-informed deep surrogate model for temperature field reconstruction of heat-source systems. Deep surrogate model is used to extract the high-level and subtle physical information to construct the temperature field. Besides, the physics-informed deep learning, which is combined by the laplace loss, the BC loss, the Point loss, and the TV loss, is developed to capture the complex physical heat transfer correlation, which makes it possible to train the deep surrogate models without labelled samples. To sum up, this works makes the following contributions.

- This work defines the temperature field reconstruction of heat-source systems (TFR-HSS) task from actual engineering applications and provides the mathematical formulation as well as the hypothesis modeling form of the task.
- Based on the hypothesis modeling of the task as well as the characteristics of prior deep regression models, this work further proposes the reversible deep model as the reconstruction models. The proposed architecture can better reconstruct the temperature field than other prior models.
- This work develops the physics-informed training losses for TFR-HSS task, including the Laplace loss for preserving physics characteristics of area without heat sources laid, the Point loss for maintaining the temperature value by transducers, the BC loss for satisfying the boundary conditions, and the TV loss for realising spatial smoothness.

Moreover, the experiments over typical two-dimensional heat-source systems have been conducted and the comparison results with the most recent methods have demonstrated the superiority of the proposed method.

The remainder of this article is organized as follows. In Section II, the mathematical model of the temperature field reconstruction task of heat-source systems is established. Section III develops the physics-informed deep surrogate models for the reconstruction task, including the deep surrogate models and the developed physics-informed training losses. The experimental studies over typical two-dimensional heat-source systems are presented to validate the effectiveness of the proposed method in Section IV. Finally, we conclude this paper with some discussions in Section V.

II. TEMPERATURE FIELD RECONSTRUCTION OF HEAT-SOURCE SYSTEMS (TFR-HSS)

This work focuses on the heat-source systems where heat may be generated internally and the principles of heat transfer are mainly concerned with. The heat-source systems can be modeled as a two-dimensional plane where each electronic component is simplified as a rectangular heat source and thermal conduction occurs along this two dimensional plane. The TFR-HSS task aims to reconstruct the overall temperature field with specified point temperature from monitoring and is the important part of real-time health detection of electronic equipment in engineering.

Generally, the mathematical formulation for temperature field reconstruction task can be formulated as

$$T^* = \arg \min_T \left(\sum_{i \in [1, m]} |T(x_{s_i}, y_{s_i} | \phi_k) - f(x_{s_i}, y_{s_i})| \right) \quad (1)$$

where $T(\cdot)$ is temperature field reconstruction model and $f(\cdot)$ is the observation temperature value. ϕ_k is the intensity distribution value of the k -th heat source. For simplicity, the intensity of each heat source is set to a constant value. O_1, O_2, \dots, O_m denote the observation points where (x_{s_i}, y_{s_i}) is the positions of the O_i observation point and m represents the number of the points.

Therefore, the key process of this specific task is to obtain the optimal temperature field using Eq. 1 while satisfying the physical equation of thermal conduction. As for the two-dimensional heat conduction, the steady-state satisfies the Laplace equation, which can be formulated as

$$\frac{\partial}{\partial x} (\lambda \frac{\partial T}{\partial x}) + \frac{\partial}{\partial y} (\lambda \frac{\partial T}{\partial y}) + \sum_{i=1}^k \phi_i(x, y) = 0 \quad (2)$$

where λ represents the thermal conductivity of the domain. k is the number of heat sources. In addition to the thermal conduction equation, physical properties over boundary conditions should also be constrained and can be generally written as

$$T = T_0 \text{ or } \lambda \frac{\partial T}{\partial \mathbf{n}} = 0 \text{ or } \lambda \frac{\partial T}{\partial \mathbf{n}} = h(T - T_0) \quad (3)$$

where T_0 is a constant temperature value, \mathbf{n} denotes the (typically exterior) normal to the boundary, and h represents the convective heat transfer coefficient. The three boundaries

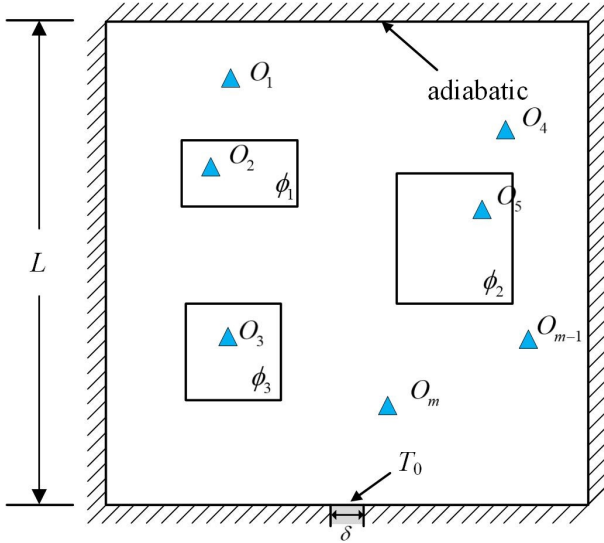


Fig. 1. The illustration of the region Ω of the heat-source systems with m sensors for temperature monitor.

are known as the Dirichlet boundary conditions (Dirichlet BCs) where T_0 is the isothermal boundary temperature, the Neumann boundary conditions (Neumann BCs) where zero heat flux is exchanged, and the Robin boundary conditions (Robin BCs) where T_0 represents the surrounded fluid temperature value. Overall, the TFR-HSS task can be transformed as the following optimization problem:

$$\begin{aligned} \min_T & \left(\sum_{i \in [1, m]} |T(x_{si}, y_{si} | \phi_k) - f(x_{si}, y_{si})| \right) \\ \text{s.t. } & \frac{\partial}{\partial x} (\lambda \frac{\partial T}{\partial x}) + \frac{\partial}{\partial y} (\lambda \frac{\partial T}{\partial y}) + \sum_{i=1}^k \phi_i(x, y) = 0 \\ & T = T_0 \text{ or } \lambda \frac{\partial T}{\partial n} = 0 \text{ or } \lambda \frac{\partial T}{\partial n} = h(T - T_0) \end{aligned} \quad (4)$$

As a representative but without loss of generality, the volume-to-point(VP) heat conduction problem in a two-dimensional rectangular domain as Fig. 1 shows is taken for the validation of the proposed methodology. In this problem, all the boundaries are adiabatic except the small patch of heat sink which is represented as δ in the figure. The reconstruction problem is modelled as typical VP problem with some heat sources distributed on a square domain (just as [16] and [19]).

Following we will introduce the proposed deep surrogate model and further develop the physics-informed deep learning methods for temperature field reconstruction.

III. PHYSICS-INFORMED DEEP SURROGATE MODEL

For convenience, Ω is used to represent the square domain. The size of the domain is set to $L = 0.1m$ and the length of the heat sink is set to $\delta = 0.01m$. Ω_e denotes the layout area without heat sources laid on. Ω_l denotes the area with heat sources laid on. Ω_b means the boundary area.

A. Numerical Modelling for TFR-HSS Task

In order to facilitate the computing process, numerical modelling of the TFR-HSS task is necessary. At first, just as Fig. 2(a) shows, the layout board for the heat-sources is meshed by $N \times N$ grid. The area in a certain grid is supposed to share a constant temperature value. The monitoring points is arranged in different grids to obtain the temperature of the grid. Then, two-dimensional matrix f of $N \times N$ with monitoring temperature can be obtained and used as the input to reconstruct the overall temperature field in the layout board. As Fig. 2(b) shows, the discretized monitoring matrix is fixed with the monitoring temperature value.

Through numerical modelling, the objective of TFR-HSS task is to obtain the temperature value of other grid in the matrix. Then, as Fig. 2(c) shows, the output of the task is the reconstructed temperature field which has been numerical modelled as a $N \times N$ matrix T . Therefore, the task can be seen as a discrete optimization problem which tries to find the surrogate mapping ϕ from monitoring matrix f to reconstructed temperature field T , and it can be written as

$$f \xrightarrow{\phi} T \quad (5)$$

Since f and T are both $N \times N$ matrix, the problem can be seen as the regression problem and general image-to-image regression methods can be applied as the deep surrogate model for the TFR-HSS task.

However, due to special characteristics of the HFR-HSS task, general deep regression methods usually cannot well work for the task. Through fully considering these characteristics, this work develops a novel reversible regression model for TFR-HSS task. Besides, considering the difficulty to obtain large amounts of labelled training samples for deep learning, this work develops the physics-informed training loss based on the physical properties of TFR-HSS task and learns the deep model unsupervisedly. Following we will introduce the proposed method detailedly.

B. Reversible Regression Model

Due to the calculation order of convolution operation in general deep regression models, the reconstructed temperature field usually has jagged boundary temperature, especially the reconstructed temperature field near the boundary of upside and rightside. The reason is that the forward and backward of convolutional layer in deep model is conducted orderly, which makes the final calculated area cannot capture the physical information.

Taking these characteristics of TFR-HSS task into consideration, this work develops the reversible regression model. Fig. 3 presents the architecture of the proposed model. As the figure shows, the proposed model, which we written as $Net_1 - Net_2$, is divided into two parts, e.g. Net_1 and Net_2 . Both Net_1 and Net_2 are independent regression model, which can have the same or different structure. Between Net_1 and Net_2 , the flip operation with diagonal flipping is conducted to ensure temperature field reconstruction of the upside and rightside boundaries.

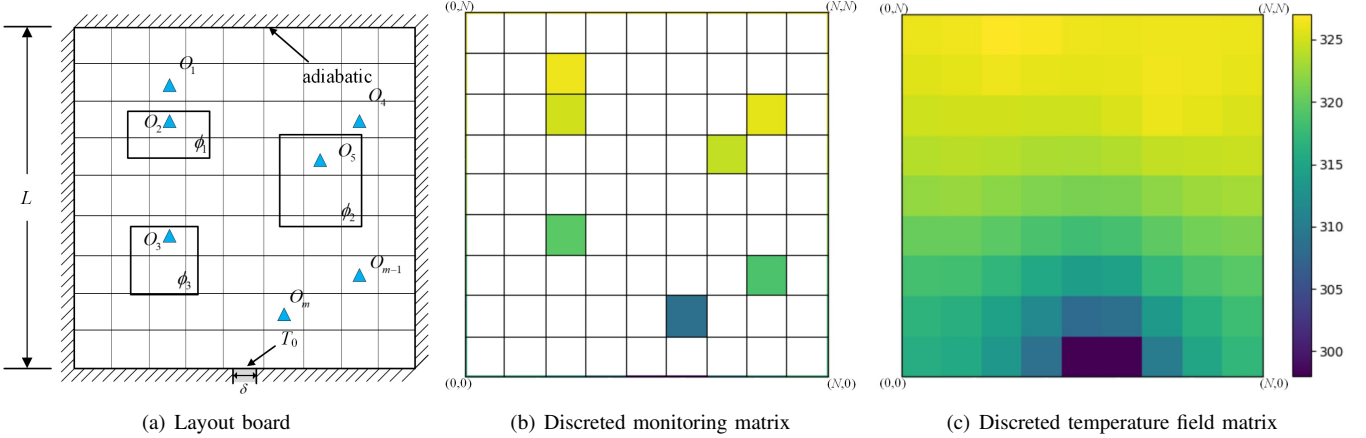
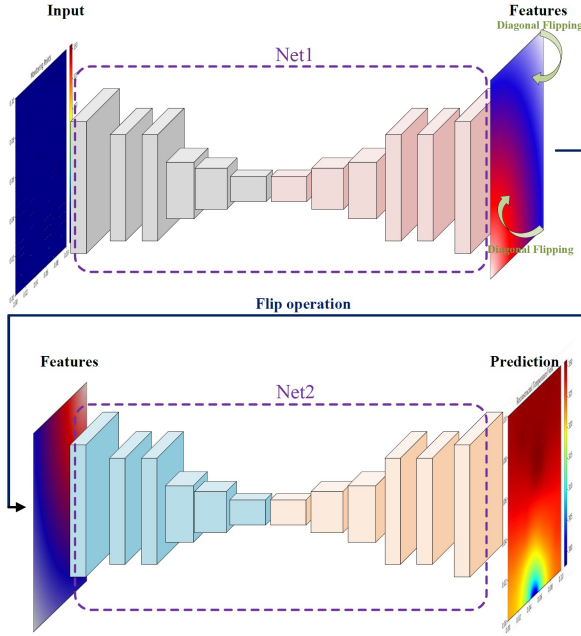


Fig. 2. Numerical modelling for TFR-HSS task.

Fig. 3. The architecture of proposed reversible regression model for the TFR-HSS task. Here, Net_1 and Net_2 represent the base models in the proposed model which can be the same deep regression model or different ones.

The proposed reversible regression model is easy to implement and can provide remarkable reconstruction performance for TFR-HSS task.

C. Physics-Informed Training Loss

Considering the characteristics of the TFR-HSS task and the strong dependency of large amounts of training samples for deep learning, this work develops the novel physics-informed reconstruction loss for the task and train the reversible regression model unsupervisedly. The loss consists of four significantly different loss terms which describe different physical characteristics from different perspectives.

First, it is generally acknowledged that MSE loss can be well work for reconstruction. In this work, we formulate the point loss L_{point} to make the predicted temperature satisfy the

temperature over monitoring points. Therefore, the point loss can be formulated as

$$L_{point} = \sum_{i=1}^m \|T(x_{s_i}, y_{s_i}) - f(x_{s_i}, y_{s_i})\|_2^2 \quad (6)$$

where $\|\cdot\|_2^2$ represents the L_2 norm.

In addition to point loss for reconstruction of monitoring points, the boundary conditions in Eq. 4 can also have significant effects on the temperature field. To use the boundary conditions for reconstruction, this work designs the BC loss L_{bc} to ensure the physical properties of the boundaries of the temperature field. Since this work mainly considers the Romann B.C. and Dirichlet B.C., the L_{bc} is formulated over this two kinds of boundary conditions separately. The Romann B.C. satisfies $\frac{\partial T}{\partial n}(x, y)|_{(x,y) \in \Omega_b^{romann}} = 0$, and the Dirichlet B.C. satisfies $T(x, y) - T_0|_{(x,y) \in \Omega_b^{dirichlet}} = 0$. Therefore, the continuous form of the L_{bc} loss can be formulated as

$$L_{bc} = |T(x, y) - T_0|_{(x,y) \in \Omega_b^{dirichlet}} + \left| \frac{\partial T}{\partial n}(x, y) \right|_{(x,y) \in \Omega_b^{romann}} \quad (7)$$

Here, the BC loss is also processed discretely. For Dirichlet B.C., the bc loss can be written as

$$L_{bc}^{Dirichlet} = \sum_{(x_i, y_j) \in \Omega_b^{dirichlet}} |T(x_i, y_j) - T_0| \quad (8)$$

For Romann B.C., the temperature over the boundary should satisfy $T(x_i, y_N) - T(x_i, y_{N-1}) = 0$ or $T(x_i, y_2) - T(x_i, y_1) = 0$ or $T(x_N, y_j) - T(x_{N-1}, y_j) = 0$ or $T(x_2, y_j) - T(x_1, y_j) = 0$. In this work, the BC loss over Romann B.C. is implemented through replicate padding the temperature field with one dimension over the surrounded boundaries. Therefore, the physical property with Romann B.C. can be satisfied through replicate padding operation, and the L_{bc} loss just requires the physical property over the Dirichlet B.C., and it can be written as

$$L_{bc} = \sum_{(x_i, y_j) \in \Omega_b^{dirichlet}} |T(x_i, y_j) - T_0|. \quad (9)$$

For the heat-source systems, the thermal conduction satisfies the two-dimensional laplace equation as Eq. 16 shows. It

builds the relationship between different point inside the heat-source systems and can guide the reconstruction of the temperature field with the help of the monitoring points. In order to take advantage of this kind of physical information, reconstruction-based Laplace loss $L_{laplace}$ is built to preserve the physical characteristics of the predicted temperature on the board where there exists no heat sources laid. The reconstruction-based laplace loss is formulated based on Eq. 16 as

$$L_{laplace} = \sum_{(x,y) \in \Omega} \left| \frac{\partial}{\partial x} \left(\lambda \frac{\partial T}{\partial x} \right) + \frac{\partial}{\partial y} \left(\lambda \frac{\partial T}{\partial y} \right) + \sum_{i=1}^k \phi_i(x, y) \right| \quad (10)$$

where λ is set to 1 in this work, namely constant thermal conductivity is assumed. Then Eq. 10 can be reformulated as

$$L_{laplace} = \sum_{(x,y) \in \Omega} \left| \frac{\partial}{\partial x} \left(\frac{\partial T}{\partial x} \right) + \frac{\partial}{\partial y} \left(\frac{\partial T}{\partial y} \right) + \sum_{i=1}^k \phi_i(x, y) \right| \quad (11)$$

For the current task, the real-time power of heat sources in the system remains unknown, and therefore in this work, the laplace loss is constructed by the thermal conduction characteristics over the domain without the heat sources laid. The continuous form of the final laplace loss $L_{laplace}$ can be written as

$$L_{laplace} = \sum_{(x,y) \in \Omega_e} \left| \frac{\partial}{\partial x} \left(\frac{\partial T}{\partial x} \right) + \frac{\partial}{\partial y} \left(\frac{\partial T}{\partial y} \right) \right| \quad (12)$$

Without exception, the laplace loss is implemented discretely. Based on the difference equation, $\frac{\partial}{\partial x} \left(\frac{\partial T}{\partial x} \right)$ can be calculated as

$$\begin{aligned} \frac{\partial}{\partial x} \left(\frac{\partial T}{\partial x} \right) &= \frac{\partial}{\partial x} \left(\frac{T(x_{i+1}, y_j) - T(x_i, y_j)}{x_{i+1} - x_i} \right) \\ &= \frac{\frac{T(x_{i+1}, y_j) - T(x_i, y_j)}{x_{i+1} - x_i} - \frac{T(x_i, y_j) - T(x_{i-1}, y_j)}{x_i - x_{i-1}}}{x_i - x_{i-1}} \end{aligned} \quad (13)$$

Since the temperature field is calculated by the uniform square mesh, the equation can be reformulated as

$$\frac{\partial}{\partial x} \left(\frac{\partial T}{\partial x} \right) \Big|_{x=x_i} = \frac{T(x_{i+1}, y_j) + T(x_{i-1}, y_j) - 2T(x_i, y_j)}{\Delta x^2} \quad (14)$$

where $\Delta x = x_{i+1} - x_i$. Similarly, $\frac{\partial}{\partial y} \left(\frac{\partial T}{\partial y} \right) \Big|_{y=y_j}$ can be reformulated as

$$\frac{\partial}{\partial y} \left(\frac{\partial T}{\partial y} \right) \Big|_{y=y_j} = \frac{T(x_i, y_{j+1}) + T(x_i, y_{j-1}) - 2T(x_i, y_j)}{\Delta y^2} \quad (15)$$

where $\Delta y = y_{j+1} - y_j$. Therefore, the discrete form of $L_{laplace}$ can be written as

$$\begin{aligned} L_{laplace} &= \sum_{(x_i, y_j) \in \Omega_e} \left| \frac{\partial}{\partial x} \left(\frac{\partial T}{\partial x} \right) \Big|_{x=x_i} + \frac{\partial}{\partial y} \left(\frac{\partial T}{\partial y} \right) \Big|_{y=y_j} \right| \\ &= \sum_{(x_i, y_j) \in \Omega_e} \left| \frac{T(x_{i+1}, y_j) + T(x_{i-1}, y_j) - 2T(x_i, y_j)}{\Delta x^2} + \right. \\ &\quad \left. \frac{T(x_i, y_{j+1}) + T(x_i, y_{j-1}) - 2T(x_i, y_j)}{\Delta y^2} \right| \end{aligned} \quad (16)$$

In the numerical processing, we set $\Delta = \Delta x = \Delta y$. Denote $D_{x_i, y_j} = T(x_{i+1}, y_j) + T(x_{i-1}, y_j) + T(x_i, y_{j+1}) + T(x_i, y_{j-1}) - 4T(x_i, y_j)$. Then, $L_{laplace}$ can be reformulated as

$$L_{laplace} = \sum_{(x_i, y_j) \in \Omega_e} \left| \frac{D_{x_i, y_j}}{\Delta^2} \right| \quad (17)$$

Interestingly, D_{x_i, y_j} is the typical two-dimensional difference format and it can be seen as a special form of convolutional operation. Therefore, in this work, $L_{laplace}$ can be calculated using convolutional operation and L_1 loss.

Generally speaking, the temperature field changes gently and there is no drastic changes. Considering such property, this work further uses the total variation (TV) regularization [20] for the temperature field reconstruction task. The TV regularization L_{tv} encourages the spatial smoothness of the predicted temperature, especially over the boundaries and the heat sources, and further helps to reconstruct the temperature field. It mainly considers the gradient information of the temperature field and can be formulated as

$$L_{tv} = \int_{\Omega} \left(\frac{\partial T}{\partial x}(x, y)^2 + \frac{\partial T}{\partial y}(x, y)^2 \right)^{\frac{\rho}{2}} \quad (18)$$

where ρ describes the order of the TV regularization. The gradient information describes the local changes of the temperature field and can be re-written as the relationship of neighboring points of the field discretely. Therefore, Eq. 18 can be calculated by

$$\begin{aligned} L_{tv} &= \sum_{i=1}^N \sum_{j=1}^N ((T(x_i, y_{j+1}) - T(x_i, y_j))^2 + \\ &\quad (T(x_{i+1}, y_j) - T(x_i, y_j))^2)^{\frac{\rho}{2}} \end{aligned} \quad (19)$$

In this work, ρ is set to 2 and the used L_{tv} can be written as

$$\begin{aligned} L_{tv} &= \sum_{i=1}^N \sum_{j=1}^N ((T(x_i, y_{j+1}) - T(x_i, y_j))^2 + \\ &\quad (T(x_{i+1}, y_j) - T(x_i, y_j))^2) \end{aligned} \quad (20)$$

Based on Eqs. 6, 9, 16, and 20, the final physics-informed reconstruction loss (PIRL) can be formulated as

$$L = L_{point} + \alpha L_{bc} + \beta L_{laplace} + \gamma L_{tv} \quad (21)$$

where α, β, γ stands for the tradeoff parameters.

D. Evaluation Metrics for the Reconstruction Performance

To evaluate the reconstruction performance of the proposed method quantitatively, this work designs the following three metrics, namely the mean absolute error (MAE), the maximum of component-constrained absolute error (M-CAE), the component-constrained mean absolute error (CMAE), and the boundary-constrained mean absolute error (BMAE).

Mean absolute error (MAE) calculates the mean absolute error of the whole reconstructed temperature field, which can be formulated as

$$E_{MAE} = \frac{1}{N^2} \sum_{i=1}^N \sum_{j=1}^N |T(x_i, y_j) - T_0(x_i, y_j)| \quad (22)$$

where T_0 represents the real temperature field obtained by numerical simulation.

Component-constrained mean absolute error (CMAE) calculates the mean absolute error of area with heat sources laid on and it can be written as

$$E_{CMAE} = \frac{1}{|\Omega_l|} \sum_{(x_i, y_j) \in \Omega_l} |T(x_i, y_j) - T_0(x_i, y_j)| \quad (23)$$

Maximum of Component-constrained absolute error (M-CAE) calculates the maximum absolute error of the whole reconstructed temperature field, which can be formulated as

$$E_{M-CAE} = \max_{(x_i, y_j) \in \Omega_l} |T(x_i, y_j) - T_0(x_i, y_j)| \quad (24)$$

Boundary-constrained mean absolute error (BMAE) calculates the mean absolute error over the boundary area and it can be written as

$$E_{BMAE} = \frac{1}{|\Omega_b|} \sum_{(x_i, y_j) \in \Omega_b} |T(x_i, y_j) - T_0(x_i, y_j)| \quad (25)$$

E. Implementation of the Proposed Method for TFR-HSS task

The pseudocode of the training process of the proposed method is given in Algorithm 1. The implementation can be divided into three parts: training process, prediction process, and evaluation process.

Step 1: Prepare the training samples, construct the reversible regression model as surrogate mapping to extract the physical information and define the hyper-parameters.

Step 2: Train the reversible regression model unsupervisedly following step 2-11 in Algorithm 1 and provide the optimized surrogate mapping ϕ^* .

Step 3: Predict the temperature field with obtained surrogate mapping ϕ^* .

Step 4: Evaluate the surrogate mapping ϕ^* under the given metrics.

IV. EXPERIMENTAL STUDIES

A. Experimental Setups

Datasets To validate the effectiveness of the proposed method for temperature field reconstruction, this work constructs four typical simulation analysis datasets with different heat sources and boundary conditions, which are described as Data A, Data B, Data C, Data D, Data A1, Data B1, Data C1, and Data D1, respectively.

As Fig. 5 shows, Data A and Data B is designed with the same heat sources layout but with different boundary conditions. Compared with Data A and Data B, Data C and Data D are designed with more complex heat sources for further analysis. In addition, Data A1 has the same heat sources layout as Data A, but with different number of monitoring points. For Data A, we set nine monitoring points on each heat source but we set only one monitoring point for Data A1. Data B1 and Data B, Data C1 and Data C, Data D1 and D have the similar settings as that on Data A1 and Data A. Table IV-A lists the number of monitoring points for these datasets. In this work, for temperature field reconstruction, the monitoring points are placed near the boundary, between the heat-sources and on the

Algorithm 1 The framework of the proposed method for TFR-HSS task

Input: Training samples $\{f_1, f_2, \dots, f_n\}$, Testing samples $\{f_{t_1}, f_{t_2}, \dots, f_{t_k}\}$, surrogate mapping ϕ , hyperparameter α, β, γ .

Output: ϕ^*

- 1: ————— Training process —————
 - 2: **while** not converge **do**
 - 3: Reconstruct the temperature field with surrogate mapping by $T_i = \phi(f_i)$ ($i = 1, 2, \dots, n$).
 - 4: Compute the point loss L_{point} using Eq. 6.
 - 5: Compute the laplace loss $L_{laplace}$ using Eq. 16.
 - 6: Compute the TV loss L_{tv} using Eq. 20.
 - 7: Compute the bc loss L_{bc} using Eq. 9.
 - 8: Compute the training loss L using Eq. 21.
 - 9: Update ϕ using training loss L by **auto-grad**.
 - 10: **end while**
 - 11: Provide the optimized surrogate mapping ϕ^* .
 - 12: ————— Prediction process —————
 - 13: Predict the temperature field of testing samples using $T_{t_i} = \phi^*(f_{t_i})$ ($i = 1, 2, \dots, k$).
 - 14: ————— Evaluation process —————
 - 15: Evaluate surrogate mapping ϕ^* under MAE, CMAE, M-CAE, and BMAE using Eq. 22-25.
 - 16: **return** ϕ .
-

heat-sources, respectively. As the table shows, 16 monitoring points are placed near the boundary. 18 points are put between components for Data A, Data B, Data A1, and Data B1 and 16 points are for Data C, Data D, Data C1, and Data D1. For Data A, B, nine monitoring points are placed on each component where for Data A1 and B1, one is placed. For Data C, D, nine monitoring points are placed for general heat sources, twelve are placed for complex sources with three parts and ten are placed for complex sources with two parts while for Data C1, D1, one is placed for general ones, three are placed for complex ones with three parts and two are placed for that with two parts.

Furthermore, the power of the heat sources in Data A and B, A1 and B1 is distributed uniformly. While in order to better evaluate the performance of the proposed method, several heat sources in Data C, D, C1 and D1 are supposed as complex power distribution. For simplicity, the complex heat source is divided into several parts (two or three in this work) and each part owes an independent uniform distributed power. For each dataset, the power of each heat source ranges from 0-30000 W/m^2 (includes different parts of the complex heat source).

For all the eight datasets, the finite element analysis (FEA) is used to generate the thermal simulation results, which are used as the groundtruth temperature field.

Optimization and hyperparameters α, β, γ are set to $1e^{-3}, 1e^{-3}, 1e^{-2}$, respectively. For each simulation data, we choose 40000 samples for training process where 80% is for training and 20% for validation, and 10000 samples for testing. The training epoch is set to 50.

Compute Infrastructure A very common machine with a 2.8-GHz Intel(R) Xeon(R) Gold 6242 CPU, 256-GB memory,

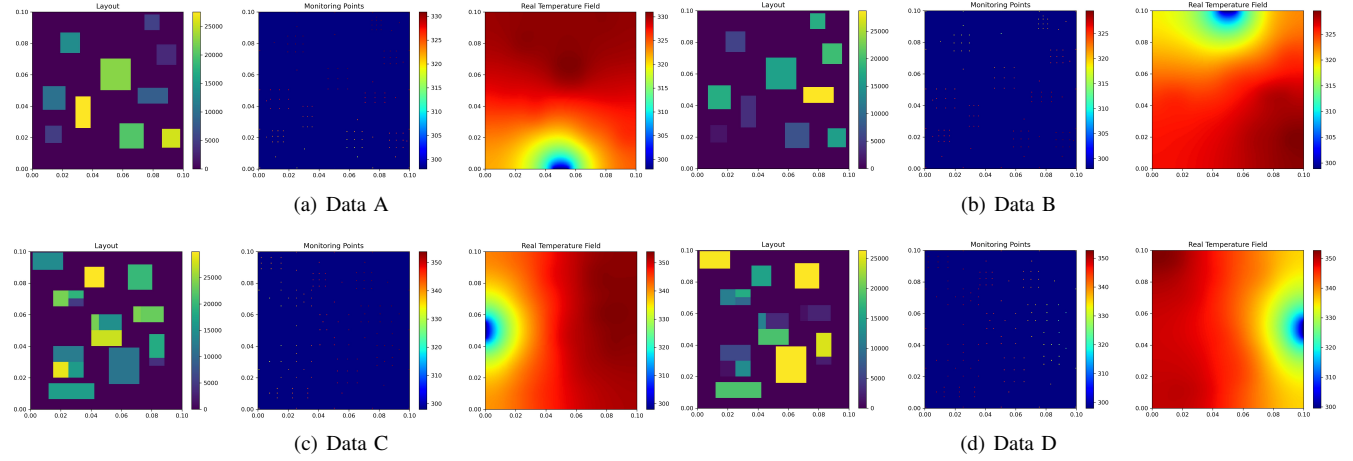


Fig. 4. Different simulation analysis datasets.

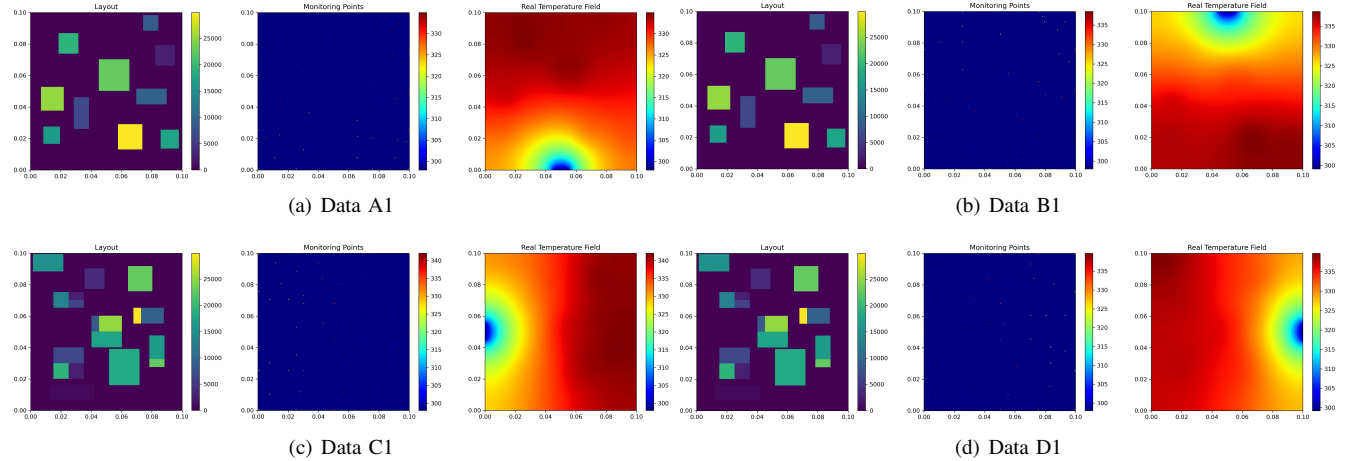


Fig. 5. Different simulation analysis datasets with less monitoring points over the heat sources in the system. Corresponding to Data A, B, C, D, Data A1, B1, C1, D1 place only one monitoring point over the component in the heat-source system.

TABLE I

NUMBER OF MONITORING POINTS USED IN THIS WORK FOR DIFFERENT DATASETS. NB, BC AND OC REPRESENT NEAR THE BOUNDARY, BETWEEN COMPONENTS AND ON THE COMPONENTS, RESPECTIVELY.

Positions	NB	BC	OC	Total
Data A & B	16	18	9×10	124
Data A1 & B1	16	18	1×10	44
Data C & D	16	16	$9 \times 5 + 12 \times 3 + 10 \times 2$	133
Data C1 & D1	16	16	$1 \times 9 + 3 \times 3 + 1 \times 2$	52

and NVIDIA GeForce RTX 3090 GPU was used to test the performance of the proposed method.

All the implementation for the TFR-HSS task was based on the Pytorch-lightning [21] deep learning framework. The codes of reproducing the proposed method for TFR-HSS task will be released soon at <https://github.com/shendu-sw/PIRL>.

B. General Reconstruction Performance

At first, we present a brief overview of the merits of the proposed physics-informed deep surrogate learning method for TFR-HSS task. In this set of experiments, the SegNet-AlexNet [22] (SegNet with AlexNet backbone) is used as the base

model of proposed reversible regression model. Both Net_1 and Net_2 in the reversible regression model uses the SegNet-AlexNet (as Fig. 8 shows).

Table II lists the performance over Data A, B, C, D under different metrics and Fig. 6 presents several reconstruction examples of the proposed method over these datasets. As the results show, the MAE of proposed method over all the datasets is less than 0.5K. Especially, over the components, the MAE is about 0.1K over all the datasets. Besides, the BMAE is about or less than 1K over all the datasets. This means that the proposed method can better reconstruct the temperature both over the components and near the boundaries. As Fig. 6 shows, the reconstruction error of only few points near

the boundaries is larger than 1K. This also indicates that the proposed reversible regression model can well work for the current task.

In the engineering, the temperature distribution over the heat sources is usually what we care most. Besides, the base models can significantly affect the performance of the proposed method. Therefore, following we will present the general reconstruction performance of the proposed method with different monitoring points on each component and the performance with different surrogate models.

1) Performance with Different Monitoring Points on Each Component: Since the temperature distribution over the heat sources is what we care most, we compare the performance of the performance with different monitoring points, that is we compare the performance between Data A and A1, B and B1, C and C1, D and D1.

Fig. 6 and 7 shows the examples of proposed method over datasets with different monitoring points over the components. Table II lists the comparison results of the proposed method over these two circumstances. Obviously, the reconstruction performance with more monitoring points over the components is better than that with less ones. The global MAE of the proposed method over Data A, B, C, D is 0.3436K, 0.2655K, 0.1727K, 0.2270K which is better than 0.5371K, 0.5437K, 0.7840K, and 0.8091K over Data A1, B1, C1, D1, respectively. Especially, The CMAE which describes the reconstruction error over the components which can obtain 0.0883K, 0.1006K, 0.1157K, 0.1153K is better than 0.4777K, 0.6210K, 0.6220K, 0.5533K. The M-CAE also shows that the proposed method can better reconstruct the temperature field with more monitoring points over the components. Compare Fig. 6 and 7, and we can find that under less monitoring points over each component, the error over the monitoring points is obvious lower than the error of other points. Especially, the reconstruction error of the neighboring points of the monitoring points is noticeably higher than that over the monitoring points. While under more monitoring points, there exists no such phenomenon and the reconstruction error is relatively uniform and very small. This means that under more monitoring points, the surrogate model obtains the physical properties of the temperature field.

Since the temperature field usually cannot achieve the expected performance with less monitoring points over components. Therefore, inspecting other methods which can reconstruct the expected temperature field with less monitoring points is urgent in the futher research. In the following, we will mainly test the performance of the proposed method over Data A, B, C, and D.

2) Performance with Different Surrogate Models: The base model of Net_1 and Net_2 in the proposed reversible regression model can significantly affect the reconstruction performance of the proposed method. In addition to the SegNet as the base model, based on the architecture of Feature Pyramid Networks (FPN) [23], Fully Convolutional Networks (FCN) [24], and UNet [25] which are proposed for general computer vision task, such as object detection [26] and image segmentation [27], this work designs several base model architectures for current task. Based on AlexNet [28], this work designs the

TABLE II
GENERAL RECONSTRUCTION PERFORMANCE (K) OF PROPOSED METHOD OVER DATASETS WITH DIFFERENT NUMBER OF MONITORING POINTS FOR TFR-HSS TASK (32000, 8000 SAMPLES FOR TRAINING, AND VALIDATION, RESPECTIVELY).

Data	MAE	M-CAE	CMAE	BMAE
Data A	0.3436	1.4340	0.0883	1.0483
Data B	0.2655	3.6059	0.1006	0.9003
Data C	0.1727	1.7394	0.1157	0.4560
Data D	0.2270	1.5093	0.1152	0.6144
Data A1	0.5371	2.1985	0.4777	0.9213
Data B1	0.5437	2.5530	0.6210	0.7909
Data C1	0.7840	4.2049	0.6220	1.5538
Data D1	0.8091	3.1192	0.5533	1.8231

specific FCN (see Fig. 10 for details) for current TFR-HSS task. Based on VGG [29], this work designs the specific UNet (see Fig. 11 for details). Based on ResNet [30], this work designs the specific FPN (see Fig. 9 for details) for this task.

In this work, we construct four forms of the proposed reversible regression models, namely Segnet-Segnet, FCN-FCN, UNet-UNet, FPN-SegNet, respectively. It should be noted that instead of FPN-FPN, we use the FPN-SegNet since the FPN-FPN does not converge for current TFR-HSS task. Table III lists the performance of the four configurations over the four datasets and Fig. 12 shows the examples of the reconstruction results over Data A with different configurations.

From the table, it can be find that FPN-SegNet performs better than other configurations over Data B and Data C under MAE while over Data, UNet-UNet performs the best and over Data D, FCN-FCN performs performs the best. From the view of M-CAE, FPN-SegNet performs the best than other configurations while under CMAE and BMAE, UNet-UNet is better than other three configurations. The SegNet-SegNet performs the worst performance among all the four configurations.

For simplicity and better presenting the performance of the proposed method affected by other variables, the SegNet-SegNet is used as the base model in the proposed method unless otherwise specified.

C. Comparisons with vanilla Deep Regression Models

In this set of experiments, we compare the proposed reversible regression model with vanilla deep regression models which are both trained by the proposed physics-informed reconstruction methods. Here, the proposed reversible regression model is divided into two forms: the reversible surrogate model with flip operation (RSM_w), and the reversible surrogate model without flip operation (RSM_{wo}).

Table IV lists the comparison results. The proposed method including the RSM_w and RSM_{wo} is better than vanilla deep regression model. Especially, the proposed method can better reconstruct the temperature field near the boundaries. From the view of BMAE, the proposed method with flip operation presents a BMAE of 1.0483K, 0.9003K, 0.4560K, 0.6144K over Data A, B, C, D, respectively, is better than the performance of vanilla regression models where the BMAE is 2.3134K, 8.2632K, 2.9737K, 12.2233K, respectively. From

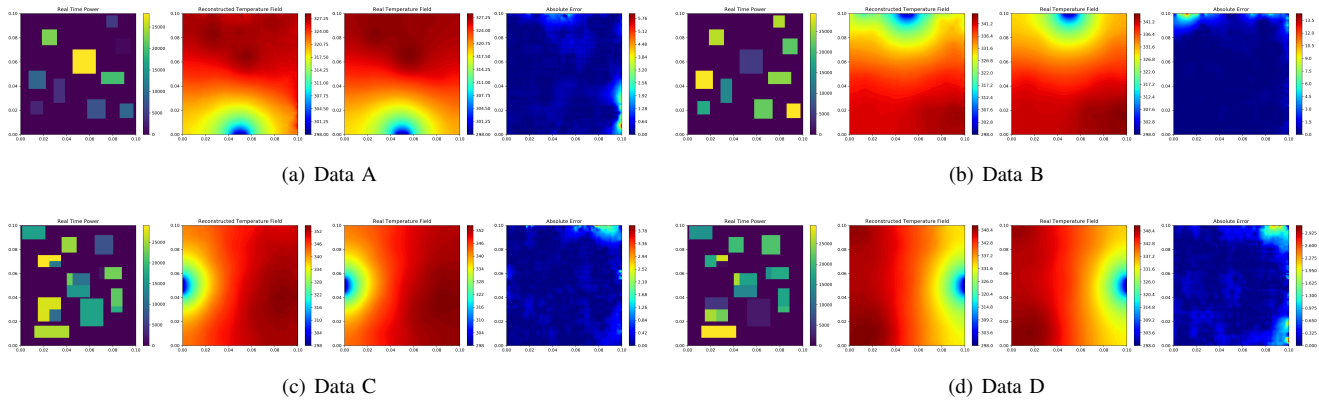


Fig. 6. Examples of proposed method over Data A, B, C and D for TFR-HSS task.

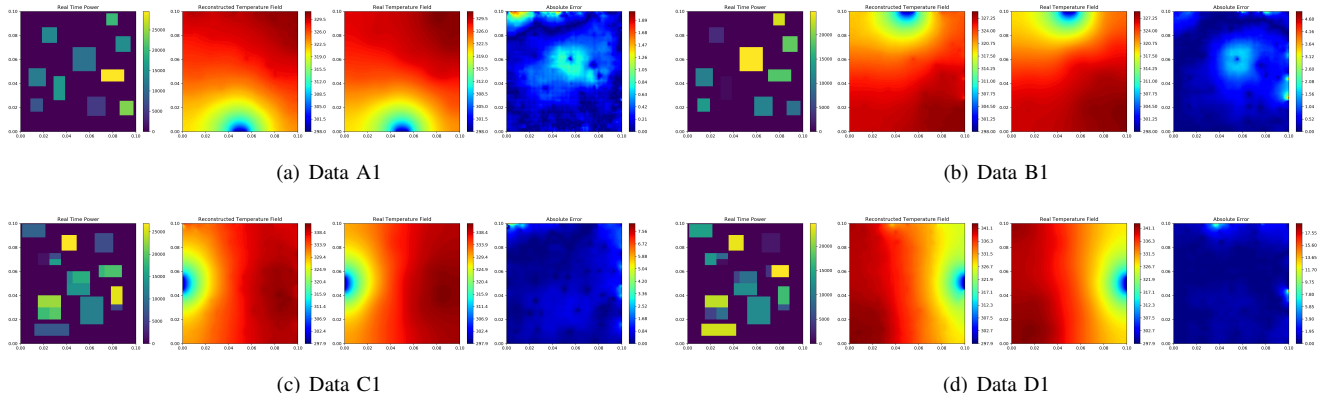


Fig. 7. Examples of proposed method over Data A1, B1, C1 and D1 which have only one monitoring point over each component for TFR-HSS task.

TABLE III
RECONSTRUCTION PERFORMANCE (K) OF PROPOSED PHYSICS-INFORMED DEEP LEARNING ON REVERSIBLE REGRESSION MODEL WITH DIFFERENT BASE MODELS FOR TFR-HSS TASK.

Models	Metrics	Data A	Data B	Data C	Data D
SegNet-SegNet	MAE	0.3436	0.2655	0.1727	0.3558
	M-CAE	1.4340	3.6059	1.7394	1.6706
	CMAE	0.0883	0.1006	0.1157	0.2103
	BMAE	1.0483	0.9003	0.4560	0.8150
FCN-FCN	MAE	0.1309	0.1605	0.1051	0.1785
	M-CAE	0.6310	0.6672	0.4913	0.7524
	CMAE	0.0865	0.1065	0.1078	0.1595
	BMAE	0.1614	0.1847	0.1589	0.2593
FPN-SegNet	MAE	0.1503	0.1510	0.0931	0.1992
	M-CAE	0.4059	0.4631	0.2941	0.4669
	CMAE	0.1429	0.1393	0.0820	0.2003
	BMAE	0.1654	0.1656	0.1502	0.2536
UNet-UNet	MAE	0.1265	0.1540	0.1146	0.2334
	M-CAE	0.3283	0.5230	0.3035	0.7550
	CMAE	0.0703	0.0983	0.0700	0.1854
	BMAE	0.1582	0.1587	0.1250	0.3098

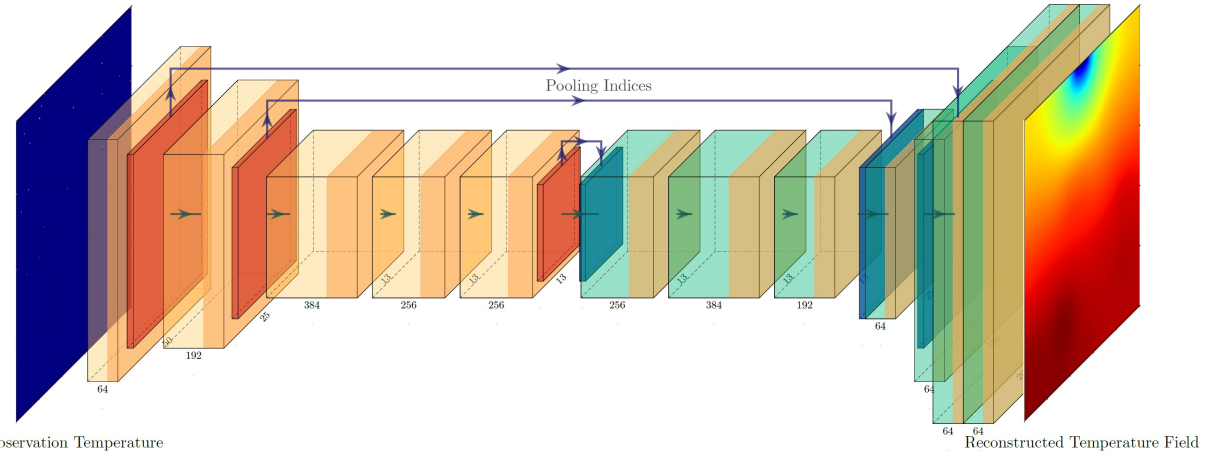


Fig. 8. The specific SegNet for TFR-HSS task.

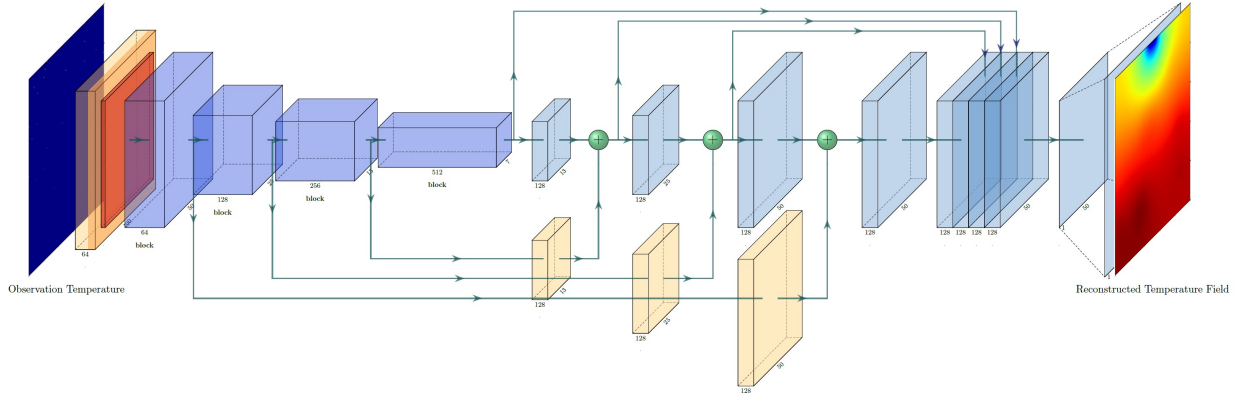


Fig. 9. The specific FPN for TFR-HSS task.

Fig. 13, it is also obvious that the proposed method can better reconstruct the temperature field, especially the field near the boundaries. Furthermore, compare the experimental results between the RSM_w and RSM_{wo} , and we can find that the flip operation can improve the reconstruction performance. This is because that the forward and backward of convolutional layer in deep model is conducted orderly, which makes the final calculated area cannot capture the physical information. Just as Fig. 13(b), 13(d), 13(f), and 13(h) shows, the temperature field near the upside and rightside boundary cannot be well reconstructed.

D. Ablation Studies

1) *Performance with Different Training Samples*: In this subsection, we conduct experiments of the proposed method with different number of training samples. The number of training samples is chosen from $\{1000, 2000, 5000, 10000, 20000, 40000\}$. Fig. 14 shows the reconstruction performance under different metrics over the four datasets.

Just the figure shows, the reconstruction performance tends to be better with the increase of the training samples. More training samples can help the proposed surrogate model to better learn the physical correlation between different points in the system. It should also be noted that when the number of

TABLE IV
RECONSTRUCTION PERFORMANCE (K) OF PROPOSED REVERSIBLE REGRESSION MODEL AND THE VANILLA DEEP REGRESSION MODEL FOR TFR-HSS TASK. IN THE TABLE, 'VANILLA' REPRESENTS THE VANILLA DEEP REGRESSION MODEL, 'RSM_{wo}' MEANS THE REVERSIBLE SURROGATE MODEL WITHOUT FLIP OPERATION AND 'RSM_w' MEANS THE REVERSIBLE SURROGATE MODEL WITH FLIP OPERATION.

Models	Metrics	Data A	Data B	Data C	Data D
Vanilla	MAE	0.7640	2.4992	0.9532	3.7638
	M-CAE	4.4597	14.1941	6.5920	35.4111
	CMAE	0.2275	0.8505	0.3544	1.4274
	BMAE	2.3134	8.2632	2.9737	12.2233
RSM_{wo}	MAE	0.5729	0.3028	0.6559	0.3658
	M-CAE	3.3061	1.8298	5.6617	1.0617
	CMAE	0.1949	0.1220	0.2570	0.1909
	BMAE	1.7699	0.8976	2.1814	0.8730
RSM_w	MAE	0.3436	0.2655	0.1727	0.2270
	M-CAE	1.4340	3.6059	1.7394	1.5093
	CMAE	0.0883	0.1006	0.1157	0.1152
	BMAE	1.0483	0.9003	0.4560	0.6144

training samples increases to a certain level, the improvement of performance tends to be slight due to the limited of the training loss as well as the deep model. This indicates that other effective training methods and representative deep models are required to extract more useful physical information

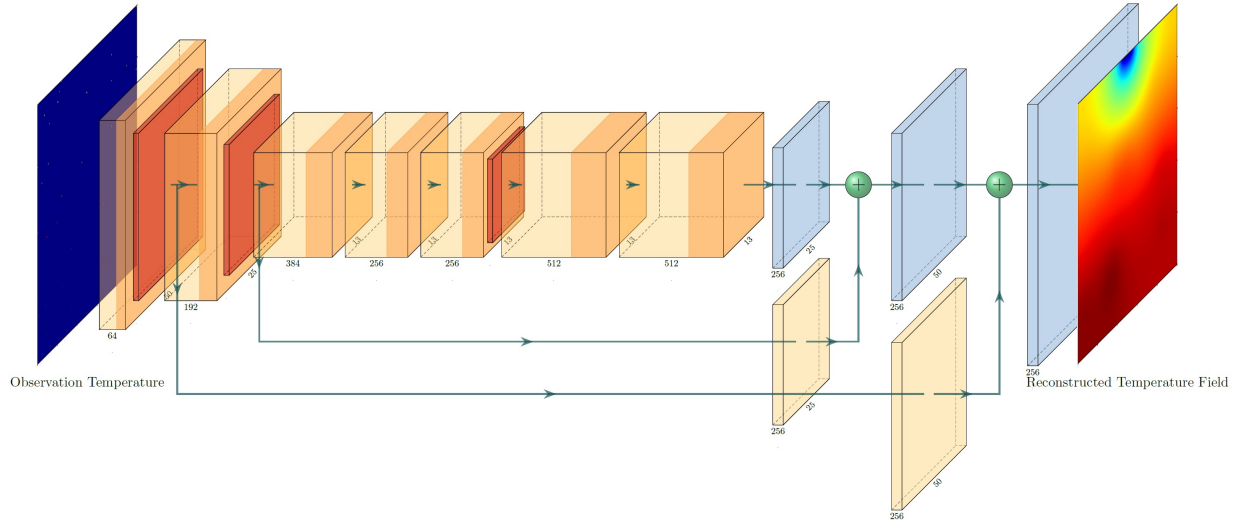


Fig. 10. The specific FCN for TFR-HSS task.

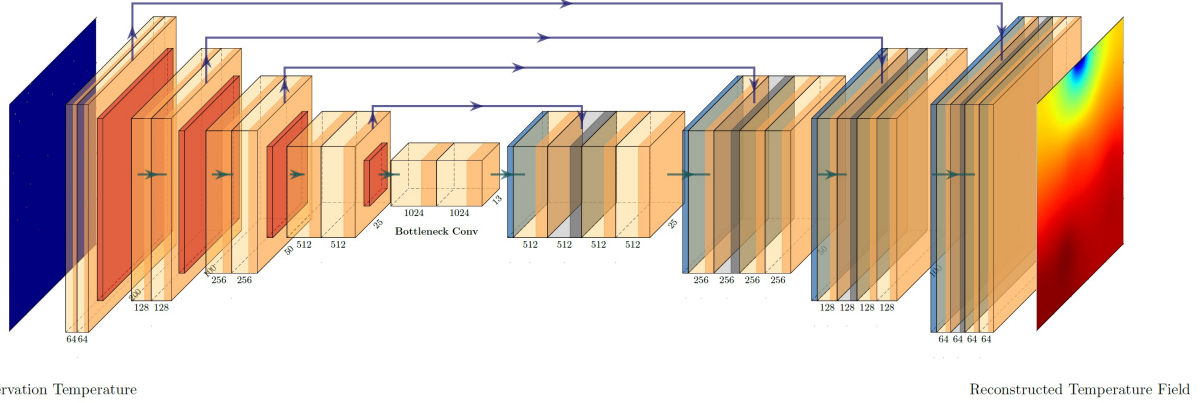


Fig. 11. The specific Unet for TFR-HSS task.

for better reconstruction performance.

2) Performance with Different Hyperparameters: In order to reconstruct the temperature field unsupervisedly with only monitoring information, the proposed method construct four different losses in order to use the physical information of temperature field, namely the Point loss, the BC loss, the Laplace loss, and the TV loss (see subsection III-C for details). These four losses play a different role in the training of the the deep model. To show the effect of different losses have on the reconstruction performance, this subsection compares the performance of the proposed method without the supervision of one of these losses.

Table V shows the comparison results where $\alpha = 0$ denotes the proposed training without BC loss, $\beta = 0$ denotes the proposed training without Laplace loss, and $\gamma = 0$ describes the proposed training without the TV loss. First of all, from the table we can find that even though some performance obtains a slight drop with the proposed method, the proposed method can help to improve the most of the performance under all these four metrics. For Data A, when $\beta = 0$ the MAE is better than the original one. We can find that when $\beta = 0$,

the BMAE tend to be 0.6108K which is significantly better than 1.0483K by original one. This means that for Data A, the slight drop of performance of original training using the laplace loss is mainly because of the BC loss instead of the laplace loss.

Inspect the reconstruction performance when $\gamma = 0$, and we can find that the TV loss which takes advantage of the neighbor correlations plays an important role in the reconstruction of temperature field near the boundary as well as the field over the component. From the table, it can be also noted that the performance drops the most without the TV loss when compared with all the other losses.

In addition, when compared the performance when $\alpha = 0$ with the original one, we can find that the BMAE drops the most. This indicates that the BC loss plays an important role in the temperature field reconstruction near the boundaries.

Overall, all the training losses in the proposed method play an important rolt in temperature field reconstruction. Under all these losses, the proposed model can better learn the physical information of temperature field and reconstruct the temperature field with expected smaller error.

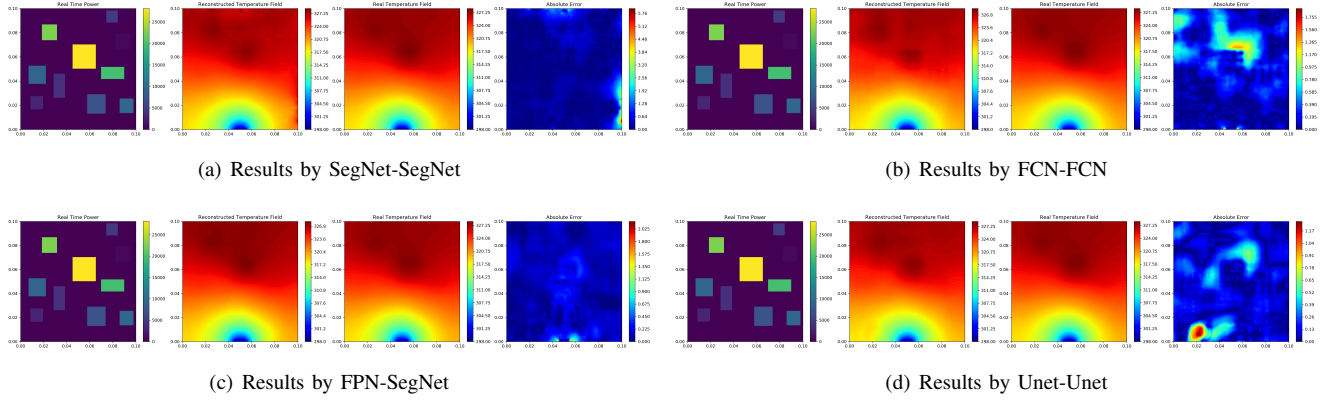


Fig. 12. Examples of the reconstruction results over Data A by proposed reversible regression models with different base models.

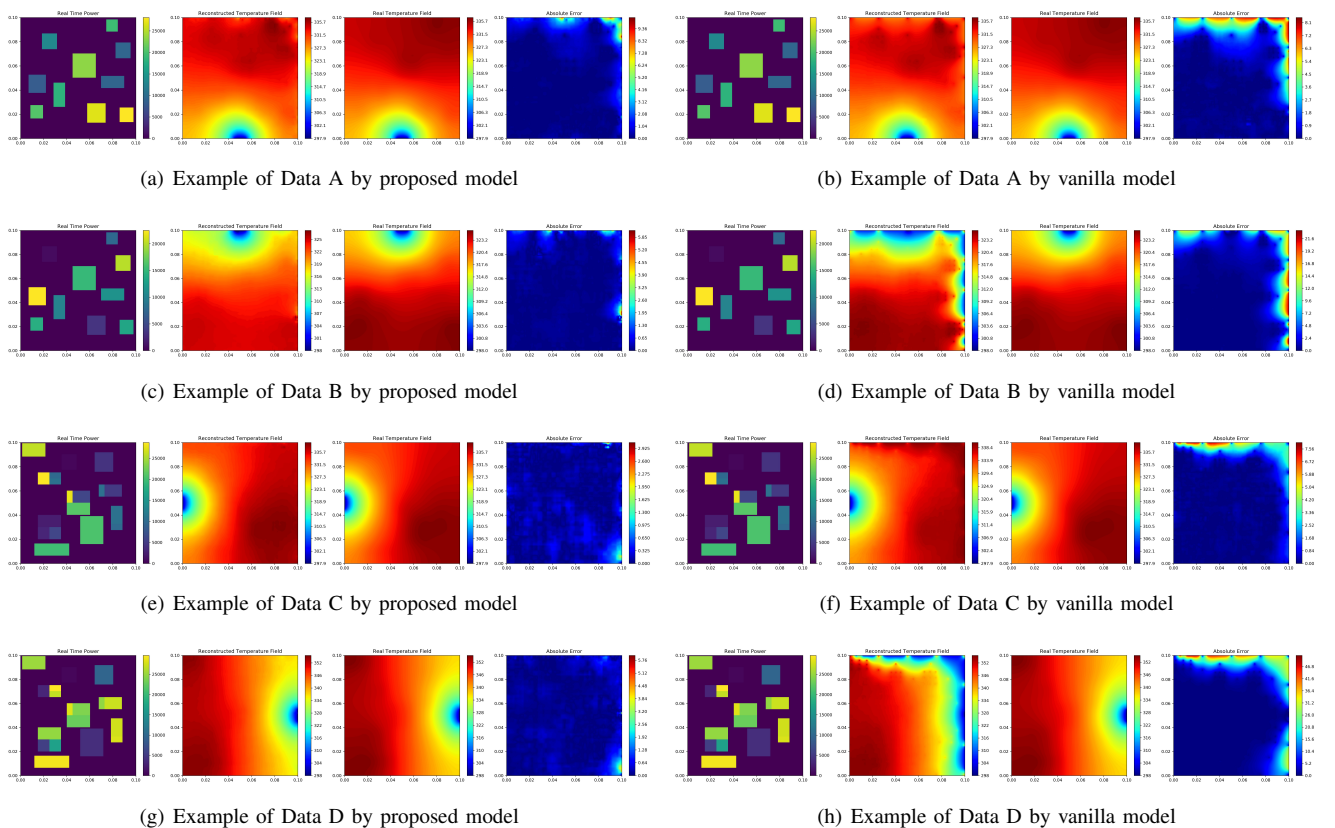


Fig. 13. Examples of the reconstruction results over different datasets by proposed reversible regression model with flip operation and vanilla deep regression model.

E. Comparisons with Other Methods

This work uses the global gaussian interpolation, Gaussian Process Regression (Kriging) [31], support vector regression [32], polynominal regression [33], neural networks (NN) [34] as baselines.

The global gaussian interpolation is proposed by us which can utilize the global information instead of the local information. The reconstructed temperature at (x_0, y_0) is related to

all the monitoring points, and it can be formulated as

$$T(x_0, y_0) = \sum_{i=1}^m \frac{e^{-|(x_0 - x_{s_i})^2 + (y_0 - y_{s_i})^2|_2}}{\sum_{j=1}^m e^{-|(x_0 - x_{s_j})^2 + (y_0 - y_{s_j})^2|_2}} f(x_{s_i}, y_{s_i}). \quad (26)$$

The Gaussian process regression is implemented with the dace toolbox. For polynomial regression, the degree of the polynomial fit is set to 5. For neural network, the structure of the network is set to '2-10-10-1'. The support vector regression is realised with the pyKriging package.

Table VI lists the comparison results with these former methods. Inspect the table and we can obtain the following

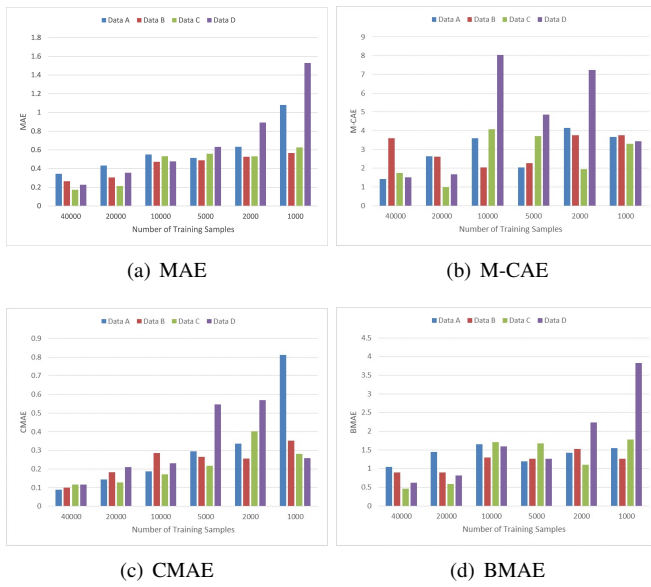


Fig. 14. Performance of proposed method with different number of unlabelled training samples for TFR-HSS task.

TABLE V
RECONSTRUCTION PERFORMANCE (K) OF PROPOSED METHOD WITH DIFFERENT HYPERPARAMETERS FOR TFR-HSS TASK.

Setting	Metric	Data A	Data B	Data C	Data D
$\alpha = 0$	MAE	0.5582	0.6050	0.6372	0.9407
$\beta = 0$		0.2144	0.5583	0.6432	0.4515
$\gamma = 0$		1.3561	1.7778	1.5841	1.9961
original		0.3436	0.2655	0.1727	0.2270
$\alpha = 0$	M-CAE	2.4146	1.4672	2.2615	3.9227
$\beta = 0$		1.3816	6.6986	4.1077	2.8034
$\gamma = 0$		9.3194	14.1046	6.9657	47.2436
original		1.4340	3.6059	1.7394	1.5093
$\alpha = 0$	CMAE	0.1471	0.1310	0.2799	0.2322
$\beta = 0$		0.1180	0.1787	0.2309	0.2319
$\gamma = 0$		0.7397	0.6592	0.6852	0.7123
original		0.0883	0.1006	0.1157	0.1152
$\alpha = 0$	BMAE	1.6682	1.5572	1.6145	3.2203
$\beta = 0$		0.6108	1.9804	1.9854	1.3210
$\gamma = 0$		3.8190	9.5846	5.5920	12.4726
original		1.0483	0.9003	0.4560	0.6144

conclusions.

First, the proposed method can obtain a better performance when compared with other methods. The proposed method can obtain a MAE of 0.1503K, 0.1510K, 0.0931K, and 0.1992K over the four datasets, respectively, outperforms all the other methods. Besides, the proposed method costs less time for prediction. Table VI shows the prediction time of 10000 samples. We can find that for all the four datasets, the proposed method costs about 50s for prediction benefiting from the use of GPUs while the fastest of other methods cost 4391.42s (NN over Data B). Especially, the SVR costs 88474.17s for prediction of Data C.

In conclusion, the proposed physics-informed deep training over reversible regression model can provide a fast prediction, provide a better reconstruction performance and be better fit for TFR-HSS task.

V. CONCLUSIONS

In this work, we give the definition of TFR-HSS task systematically and further develop the physics-informed deep surrogate model for the task. First, a novel two stage deep surrogate model is proposed for the TFR-HSS task. Experiments have shown that the proposed two stage deep surrogate model can better reconstruct the temperature field on the boundary than general deep regression models. Then, we develop a novel physics-informed deep surrogate model for TFR-HSS task, including the laplace loss, the point loss, the bc loss and the tv loss. With the proposed method, the deep surrogate model can be trained unsupervisedly. The experimental results also demonstrate that the temperature field can be well reconstructed. Besides, compared with commonly used kriging method and other machine learning methods, the proposed method can provide better reconstruction performance.

As future work, it would be interesting to design the special layer which can better extract the intrinsic physical properties for TFR-HSS task. Besides, investigating other physics-informed training loss which can better train the deep surrogate model is another interesting topic. Reducing redundant monitoring points while maintaining the reconstruction performance is also worthy of deep study.

REFERENCES

- [1] M. Gruijicic, C. L. Zhao, and E. C. Dusel, "The effect of thermal contact resistance on heat management in the electronic packaging," *Applied Surface Science*, vol. 246, pp. 290–302, 2005.
- [2] E. Laloya, O. Lucia, H. Sarnago, and J. M. Burdio, "Heat management in power converters: From state of the art to future ultrahigh efficiency systems," *IEEE Transactions on Power Electronics*, vol. 31, no. 11, pp. 7896–7908, 2015.
- [3] K. V. L. Narayana and V. N. Kumar, "Development of an intelligent temperature transducer," *IEEE Sensors Journal*, vol. 16, no. 12, pp. 4696–4703, 2016.
- [4] G. C. M. Meijer, R. Van Gelder, V. Nooder, and et al, "A three-terminal intergrated temperature transducer with microcomputer interfacing," *Sensors and Actuators*, vol. 18, no. 2, pp. 195–206, 1989.
- [5] M. Chirtoc, J. Bodzenta, and A. Kazmierczak-Balata, "Calibration of conductance channels and heat flux sharing in scanning thermal microscopy combining resistive thermal probes and pyroelectric sensors," *International Journal of Heat and Mass Transfer*, vol. 156, pp. 1–13, 2020.
- [6] L. Massa and J. A. Schetz, "Hypersonic heat flux reconstruction with distributed temperature sensors," *Journal of Thermophysics and Heat Transfer*, vol. 34, no. 2, pp. 331–346, 2020.
- [7] A. Capozzoli, C. Curcio, A. Liseno, and et al, "Field sampling and field reconstruction: A new perspective," *Radio Science*, vol. 45, no. 06, pp. 1–31, 2010.
- [8] R. Kress, *Interpolation*. New York: Springer, 1998.
- [9] B. D. Lackey, M. Purrer, A. Taracchini, and et al, "Surrogate for an aligned-spin effective-one-body waveform model of binary neutron star inspirals using gaussian process regression," *Physical Review D*, vol. 100, no. 2, p. 024002, 2019.
- [10] N. D. Le and J. V. Zidek, *Statistical analysis of environmental space-time processes*. Springer Science & Business Media, 2006.
- [11] S. C. Leu, Z. Huang, and Z. Lin, "Generation of pseudo-ct using high-degree polynomial regression on dual-contrast pelvic mri data," *Scientific Reports*, vol. 10, no. 1, pp. 1–11, 2020.
- [12] T. Ma, Y. Liu, and C. Cao, "Neural networks for 3d temperature field reconstruction via acoustic signals," *Mechanical Systems and Signal Processing*, vol. 126, pp. 392–406, 2019.
- [13] J. Lei and S. Liu, "Temperature field reconstruction from the partial measurement data using the gappy proper orthogonal decomposition," *IET Science, Measurement and Technology*, vol. 7, no. 3, pp. 171–179, 2013.

TABLE VI
RECONSTRUCTION PERFORMANCE (K) OF DIFFERENT METHODS FOR TFR-HSS TASK.

Data	Method	Prediction Time (s)	MAE	M-CAE	CMAE	BMAE
Data A	Global Gaussian Interpolation	13884.73s	0.6148	3.3857	1.4215	2.6057
	Gaussian Process Regression	8596.87s	0.2799	1.2582	0.5800	2.4980
	Support Vector Regression (SVR)	36164.35s	0.2703	0.5196	0.0707	2.9585
	Polynomial Regression	16421.41s	0.5852	1.6478	1.3492	6.2793
	Neural Networks (NN)	4411.96s	0.4844	3.5185	1.1381	3.6544
	Proposed Method (FPN-based)	52s	0.1503	0.4059	0.1429	0.1654
Data B	Global Gaussian Interpolation	14143.03s	0.7128	13.5829	2.6513	3.2147
	Gaussian Process Regression	8783.92s	0.3026	5.3661	1.0045	2.1256
	Support Vector Regression (SVR)	30420.54s	0.3190	0.4985	0.0698	3.6980
	Polynomial Regression	16766.82s	0.6410	6.2734	2.0138	5.9980
	Neural Networks (NN)	4391.42s	0.5188	9.2131	1.7123	3.4599
	Proposed Method (FPN-based)	47s	0.1510	0.4631	0.1393	0.1656
Data C	Global Gaussian Interpolation	16517.52s	0.7693	19.3481	2.4615	3.6707
	Gaussian Process Regression	11754.00s	0.2998	7.9193	0.8648	2.0172
	Support Vector Regression (SVR)	88474.17s	0.2563	0.3905	0.0711	3.5960
	Polynomial Regression	18569.39s	0.7478	9.0079	1.7457	8.8377
	Neural Networks (NN)	6796.88s	0.6091	13.6171	1.6593	5.1221
	Proposed Method (FPN-based)	47s	0.0931	0.2941	0.0820	0.1502
Data D	Global Gaussian Interpolation	16812.54s	0.6292	3.8791	1.3781	3.1352
	Gaussian Process Regression	11673.16s	0.2447	2.7767	0.5321	3.3184
	Support Vector Regression (SVR)	73571.12s	0.2520	0.3934	0.0661	3.9598
	Polynomial Regression	18654.51s	0.8267	2.7283	1.6437	8.1815
	Neural Networks (NN)	6857.72s	0.6081	3.9741	1.2454	4.9797
	Proposed Method (FPN-based)	47s	0.1992	0.4669	0.2003	0.2536

- [14] Z. Gong, P. Zhong, Y. Yu, and et al, “A cnn with multiscale convolution and diversified metric for hyperspectral image classification,” *IEEE Transactions on Geoscience and Remote Sensing*, vol. 57, no. 6, pp. 3599–3618, 2019.
- [15] Z. Gong, P. Zhong, and W. Hu, “Statistical loss and analysis for deep learning in hyperspectral image classification,” *IEEE Transactions on Neural Networks and Learning Systems*, vol. 32, no. 1, pp. 322–333, 2021.
- [16] X. Chen, X. Zhao, Z. Gong, and et al, “A deep neural network surrogate modeling benchmark for temperature field prediction of heat source layout,” *arXiv preprint arXiv:2103.11177*, 2021.
- [17] H. K. Aggarwal, M. P. Mani, and M. Jacob, “Modl: Model-based deep learning architecture for inverse problems,” *IEEE Transactions on Medical Imaging*, vol. 38, no. 2, pp. 394–405, 2018.
- [18] Z. Gong, W. Hu, X. Du, and et al, “Deep manifold embedding for hyperspectral image classification,” *IEEE Transactions on Cybernetics*, 2021.
- [19] Y. Aslan, J. Puskely, and A. Yarovoy, “Heat source layout optimization for two-dimensional heat conduction using iterative reweighted 11-norm convex minimization,” *International Journal of Heat and Mass Transfer*, vol. 122, pp. 432–441, 2018.
- [20] L. I. Leonid, S. Osher, and E. Fatemi, “Nonlinear total variation based noise removal algorithms,” *Physica D: Nonlinear Phenomena*, vol. 60, pp. 259–268, 1992.
- [21] W. A. Falcon, “Pytorch lightning,” <https://github.com/williamFalcon/pytorch-lightning>, 2021, accessed May 24, 2021.
- [22] V. Badrinarayanan, A. Kendall, and R. Cipolla, “Segnet: A deep convolutional encoder-decoder architecture for image segmentation,” *IEEE Transactions on Pattern Analysis and machine Intelligence*, vol. 39, no. 12, pp. 2481–2495, 2017.
- [23] T. Y. Lin, P. Dollar, R. Girshick, K. He, B. Hariharan, and S. Belongie, “Feature pyramid networks for object detection,” in *Proceedings of the IEEE Conference on Computer Vision and Pattern Recognition*, 2017, pp. 2117–2125.
- [24] J. Long, E. Shelhamer, and T. Darrell, “Fully convolutional networks for semantic segmentation,” in *Proceedings of the IEEE Conference on Computer Vision and Pattern Recognition*, 2015, pp. 3431–3440.
- [25] O. Ronneberger, P. Fischer, and T. Brox, “U-net: Convolutional networks for biomedical image segmentation,” in *International Conference on Medical Image Computing and Computer-assisted Intervention*, 2015, pp. 234–241.
- [26] Z. Q. Zhao, P. Zheng, S. T. Xu, and X. Wu, “Object detection with deep learning: A review,” *IEEE Transactions on Neural Networks and Learning Systems*, vol. 30, no. 11, pp. 3212–3232, 2019.
- [27] S. Minaee, Y. Y. Boykov, F. Porikli, A. J. Plaza, N. Kehtarnavaz, and D. Terzopoulos, “Image segmentation using deep learning: A survey,” *IEEE Transactions on Pattern Analysis and Machine Intelligence*, 2021.
- [28] A. Krizhevsky, I. Sutskever, and G. E. Hinton, “Imagenet classification with deep convolutional neural networks,” in *Advances in Neural Information Processing Systems*, vol. 25, 2012, pp. 1097–1105.
- [29] K. Simonyan and A. Zisserman, “Very deep convolutional networks for large-scale image recognition,” in *International Conference on Learning Representations*, 2015.
- [30] K. He, X. Zhang, S. Ren, and J. Sun, “Deep residual learning for image recognition,” in *Proceedings of the IEEE Conference on Computer Vision and Pattern Recognition*, 2016, pp. 770–778.
- [31] E. Schulz, M. Speekenbrink, and A. Krause, “A tutorial on gaussian process regression: Modelling, exploring, and exploiting functions,” *Journal of Mathematical Psychology*, vol. 85, pp. 1–16, 2018.
- [32] M. Awad and R. Khanna, *Efficient learning machines*. Berkeley, CA: Apress, 2015.
- [33] E. Ostertagova, “Modelling using polynomial regression,” *Procedia Engineering*, vol. 48, pp. 500–506, 2012.
- [34] S. Haykin, *Neural Networks and Learning Machines*. New York: Prentice Hall, 2009.

Zhiqiang Gong received the B.S. degree in applied mathematics from Shanghai Jiao Tong University, Shanghai, China, in 2013, the M.S. degree in applied mathematics from the National University of Defense Technology (NUDT), Changsha, China, in 2015, and the Ph.D. degree in information and communication engineering from the National Key Laboratory of Science and Technology on ATR, NUDT, in 2019.

He is currently an Assistant Professor with the National Innovation Institute of Defense Technology, Chinese Academy of Military Science, Beijing, China. He has authored more than ten peer-reviewed articles in international journals, such as the IEEE TRANSACTIONS ON NEURAL NETWORKS AND LEARNING SYSTEMS, the IEEE TRANSACTIONS ON CYBERNETICS, the IEEE TRANSACTIONS ON GEOSCIENCE AND REMOTE SENSING, the IEEE GEOSCIENCE AND REMOTE SENSING LETTERS, and the IEEE JOURNAL OF SELECTED TOPICS IN APPLIED EARTH OBSERVATIONS AND REMOTE SENSING. His research interests are computer vision, machine learning, model-based deep learning, pattern recognition, and image analysis.